J. Fluid Mech. (2002), *vol.* 450, *pp.* 259–285.
DOI: 10.1017/S0022112001006437 Printed in the United Kingdom

Direct numerical simulation of turbulent channel flow with permeable walls

By SEONGHYEON HAHN, JONGDOO JE† AND HAECHEON CHOI‡

School of Mechanical and Aerospace Engineering, Seoul National University, Seoul 151-742, Korea

(Received 11 February 2000 and in revised form 25 February 2001)

The main objectives of this study are to suggest a proper boundary condition at the interface between a permeable block and turbulent channel flow and to investigate the characteristics of turbulent channel flow with permeable walls. The boundary condition suggested is an extended version of that applied to laminar channel flow by Beavers & Joseph (1967) and describes the behaviour of slip velocities in the streamwise and spanwise directions at the interface between the permeable block and turbulent channel flow. With the proposed boundary condition, direct numerical simulations of turbulent channel flow that is bounded by the permeable wall are performed and significant skin-friction reductions at the permeable wall are obtained with modification of overall flow structures. The viscous sublayer thickness is decreased and the near-wall vortical structures are significantly weakened by the permeable wall. The permeable wall also reduces the turbulence intensities, Reynolds shear stress, and pressure and vorticity fluctuations throughout the channel except very near the wall. The increase of some turbulence quantities there is due to the slip-velocity fluctuations at the wall. The boundary condition proposed for the permeable wall is validated by comparing solutions with those obtained from a separate direct numerical simulation using both the Brinkman equation for the interior of a permeable block and the Navier–Stokes equation for the main channel bounded by a permeable block.

1. Introduction

The flow in a channel surrounded by a permeable medium has significant importance in various areas of engineering because many industrial processes are associated with the phenomena occurring in this flow. Examples include the manufacturing process of advanced composites, oil recovery, and underground water flow. Therefore, a large number of studies have been made so far, especially on the accurate prediction of various flow phenomena inside and over a permeable medium, because the precise description of the flow is essential in understanding the associated transport phenomena. Although Darcy's well-known law is useful and sufficient for predicting bulk flow, detailed transport phenomena near the boundary of a permeable block

† Present address: Engine Engineering Center, Samsung Techwin Co., Ltd., Changwon 641-717, Korea.

‡ Author to whom correspondence should be addressed: e-mail choi@socrates.snu.ac.kr. Also at National CRI Center for Turbulence and Flow Control Research, Institute of Advanced Machinery and Design, Seoul National University.

cannot be captured merely by it. Therefore, a more sophisticated flow model should be considered to precisely represent this boundary layer.

Traditionally, flow near a permeable interface had been modelled by Brinkman's modification of Darcy's law, where a linear combination of the Stokes equation for microscopic pore-level flow and Darcy's law for the bulk resistance was used (Brinkman 1947). Although it is still uncertain how to determine the viscosity of the whole fluid-filled permeable matrix (which is called the effective viscosity) when using Brinkman's equation, Brinkman's modification is in general regarded as a plausible extension of Darcy's law for a uniformly dilute permeable matrix under the condition that effects of the boundary or interface are not significant, because theoretically more rigorous attempts to reach a universal governing equation for the flow in a permeable medium by the ensemble- or local volume-averaging of the microscopic pore-level flows also lead to an equation in a similar form to Brinkman's (Slattery 1969; Saffman 1971; Lundgren 1972; Whitaker 1986). The usefulness of Brinkman's equation was shown by Neale & Nader (1974*a*) with the effective viscosity assumed to be the fluid viscosity (which was originally suggested by Brinkman). For theoretical approaches to determine the effective viscosity as a function of the porosity as well as the fluid viscosity, see Lundgren (1972) and Koplik, Levine & Zee (1983).

However, the applicability of Brinkman's equation to the flow near the permeable interface has been questioned: Sahraoui & Kaviany (1992) performed a direct pore-level simulation and showed that the prediction performance of Brinkman's equation near the permeable boundary depends significantly on the microscopic pore structure and thus the equation can be quite erroneous, especially in predicting the correct thickness of the boundary layer formed near the permeable interface, which was also shown by Gupte & Advani's (1997) experimental work using LDA measurements. Moreover, Kaviany (1987) showed through an analysis of Vafai & Tien's (1981) slightly different version of Brinkman's equation that a Brinkman-type equation can yield a boundary layer thickness smaller than the diameter of a pore in the porous medium where the Carman–Kozeny relation holds, which violates the fundamental assumption of the local volume-averaging technique. Although Sahraoui & Kaviany (1992) also proposed some remedies by determining the effective viscosity as a function of space, their suggestions were based on pore-level simulations with extremely simplified pore structures (two-dimensional in-line or staggered arrays of cylinders) and so still has a limitation for direct application to real permeable matrices with complex pore geometry. Therefore, a more general treatment of the permeable boundary is required.

On the other hand, if the main interest lies in the outer channel flow rather than in the flow inside the permeable wall itself, a different approach is possible, in which the interaction between the outer channel flow and the permeable wall is modelled as a boundary condition. Beavers & Joseph (1967) proposed a slip-boundary condition at the interface between a permeable block and laminar channel flow and derived an analytic solution of the flow. They also verified their slip-boundary condition by comparing the analytic solution with their experimental work. Saffman (1971) also proved the slip-boundary condition suggested by Beavers & Joseph to be valid from his theoretical work. Sahraoui & Kaviany (1992) showed that unlike Brinkman's equation, the slip-boundary condition of Beavers & Joseph properly describes the flow phenomenon with a proper value of the slip coefficient α. Gupte & Advani (1997) experimentally showed that there exists a slip velocity in the main-flow direction at the interface between the permeable block and laminar channel flow, which is consistent with the slip-boundary condition of Beavers & Joseph, while Brinkman's

equation is erroneous in estimating the correct screening depth of the boundary layer into the permeable block. In spite of the difficulty of assigning a precise value for the non-dimensional slip coefficient α, the slip-boundary condition of Beavers & Joseph has been proved to properly describe the physical phenomena of laminar channel flow above the permeable wall.

Recent manufacturing processes and some other engineering applications include turbulent flows that interact with a permeable block (Antohe & Lage 1997). In combustion processes, for instance, the use of porous inert media leads to a reduction in gas temperature and consequently to a reduction of NO_X emissions. Evidently, turbulence affects the transport phenomena and combustion significantly. Another important practical application is the prediction of contaminant transport by wind through forests and crops, which is generally modelled as flow through porous media. The geometric dimensions and fluid speed are sufficient for generating turbulence. For this reason, understanding the characteristics of turbulent flow above a permeable wall becomes important and thus an accurate boundary condition that describes the flow phenomenon at the interface between the permeable block and outer turbulent flow should be investigated.

Recently, Perot & Moin (1995) investigated turbulent flow above a 'perfectly' permeable wall using the direct numerical simulation technique. Their objective was to investigate the modification of flow characteristics in the absence of the blocking effect of a no-slip wall, and thus they allowed the fluid to freely permeate through the surface, i.e. $\partial v/\partial y = 0$ rather than $v = 0$ on the wall, where y is the wall-normal direction and v is the wall-normal velocity. Wagner & Friedrich (1997) applied the same boundary condition to a turbulent pipe flow and reported a significant drag increase. In most manufacturing processes, however, permeable blocks are confined in the overall system so that the freely permeable condition for the wall-normal velocity may not be realized. Therefore, the definition of the permeable wall pursued in this study is completely different from that of Perot & Moin.

The objectives of the present study are to suggest a proper boundary condition at the interface between turbulent channel flow and a permeable block, which is an extended version of Beavers & Joseph's (1967), and to investigate the characteristics of the flow. The boundary condition suggested for the permeable wall is applied to fully developed turbulent channel flow with varying permeability k and the resulting flow fields are compared with turbulent channel flow with a no-slip wall. Numerical procedures are presented in § 2. The boundary condition for the permeable wall is given in § 3. Variations of drag and velocity profiles due to the permeable wall are presented in § 4 and turbulence statistics are provided in § 5. Finally, validation of the proposed boundary condition is presented in § 6, followed by summary in § 7.

2. Numerical procedures

The governing equations are the unsteady incompressible three-dimensional Navier–Stokes equations and the continuity equation

$$\frac{\partial u_i}{\partial t} + \frac{\partial}{\partial x_j} u_i u_j = -\frac{\partial p}{\partial x_i} + \frac{1}{Re} \frac{\partial}{\partial x_j} \frac{\partial u_i}{\partial x_j}, \tag{1}$$

$$\frac{\partial u_i}{\partial x_i} = 0, \tag{2}$$

where t is the time, x_i are the spatial coordinates, u_i are the corresponding velocity components and p is the pressure. All variables are normalized by the channel half-

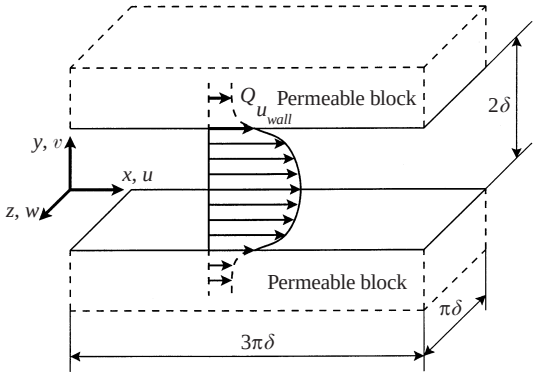

FIGURE 1. Schematic diagram of the flow geometry.

width δ and the laminar centreline velocity u_c, and the Reynolds number is defined as $Re = u_c\delta/v$, where v is the kinematic viscosity.

To solve (1) and (2), a semi-implicit, fractional step method is used (Kim & Moin 1985; Le & Moin 1991):

$$\frac{\hat{u}_i^m - u_i^{m-1}}{\Delta t} = \beta_m(\hat{L}_i^m + L_i^{m-1}) - (\gamma_m + \rho_m)\frac{\partial p^{m-1}}{\partial x_i} - \gamma_m N_i^{m-1} - \rho_m N_i^{m-2}, \tag{3}$$

$$(\gamma_m + \rho_m)\frac{\partial}{\partial x_i}\frac{\partial \phi^m}{\partial x_i} = \frac{1}{\Delta t}\frac{\partial \hat{u}_i^m}{\partial x_i}, \tag{4}$$

$$\frac{u_i^m - \hat{u}_i^m}{\Delta t} = -(\gamma_m + \rho_m)\frac{\partial \phi^m}{\partial x_i}, \tag{5}$$

with

$$L_i = \frac{1}{Re}\frac{\partial}{\partial x_j}\frac{\partial u_i}{\partial x_j}, \qquad N_i = \frac{\partial}{\partial x_j}u_i u_j, \tag{6}$$

where m is the substep index of a third-order Runge–Kutta method ($m = 1, 2, 3$), $\beta_1 = \frac{4}{15}$, $\beta_2 = \frac{1}{15}$, $\beta_3 = \frac{1}{6}$, $\gamma_1 = \frac{8}{15}$, $\gamma_2 = \frac{5}{12}$, $\gamma_3 = \frac{3}{4}$, $\rho_1 = 0$, $\rho_2 = -\frac{17}{60}$ and $\rho_3 = -\frac{5}{12}$. Here, the convection term is advanced with a third-order Runge–Kutta method and the Crank–Nicolson method is used for the diffusion term. The relation between p and ϕ is given as

$$p^m = p^{m-1} + \phi^m - \frac{\beta_m \Delta t}{Re}\nabla^2 \phi^m. \tag{7}$$

All the spatial derivatives are discretized with the second-order central-difference scheme.

The channel flow geometry and coordinate system are shown in figure 1. The upper and lower walls are bounded by permeable blocks. Fully developed turbulent channel flow with permeable walls is homogeneous in the streamwise (x) and spanwise (z) directions, and periodic boundary conditions are used in the x- and z-directions. The boundary condition that describes the permeable wall is presented in the following section. The computations are carried out maintaining a constant mass flow rate in the channel for a Reynolds number of 3000 based on the laminar centreline velocity u_c and channel half-width δ (the Reynolds number based on the bulk mean velocity and the full channel width is 4000), which corresponds to a Reynolds number of about 140 based on the wall-shear velocity $u_{\tau_{im}}$ at the impermeable wall and channel half-width. The streamwise and spanwise computational periods are $3\pi\delta$ and $\pi\delta$, respectively.

The number of grid points is $64 \times 97 \times 96$ in the streamwise, wall-normal and spanwise directions. Uniform grids are used in the streamwise and spanwise directions and the consequent grid spacings in wall units are $\Delta x^+ \approx 20.3$ and $\Delta z^+ \approx 4.5$. In the wall-normal direction, non-uniform grids are constructed by using a hyperbolic tangent function ($\Delta y^+ = 0.3$–6.6). The spatial resolutions used in this study are very similar to those in Kim, Moin & Moser (1987). It was shown in Choi, Moin & Kim (1992) that when the second-order central-difference scheme is used, the same number of grid points as for the spectral method is sufficient to have a spectral resolution of the turbulence intensities and Reynolds shear stress, but there is a slight under- or over-prediction of the vorticity fluctuations. The CFL number is fixed to be 1.0, which corresponds to $\Delta t^+ = \Delta t u_{\tau_{im}}^2 / \nu \approx 0.37$. It was shown by Choi & Moin (1994) that a computational time step of less than $\Delta t^+ \approx 0.4$ accurately predicts turbulence statistics in a turbulent channel flow.

3. Boundary condition for the permeable wall

3.1. *Previous work on the boundary condition for the permeable wall*

Among many other boundary conditions describing the permeable wall, Beavers & Joseph (1967) reported a slip-boundary condition for laminar channel flow and introduced a non-dimensional parameter α, called the slip coefficient, in addition to the permeability k that has the physical dimension of $[L^2]$. They verified the slip-boundary condition by comparing their analytic solution with their experimental result for laminar channel flow. They used Darcy's law as follows to formulate the flow in the interior of the permeable block:

$$Q = -\frac{k}{\mu}\frac{\mathrm{d}p}{\mathrm{d}x}, \tag{8}$$

where Q is the mean filtered velocity (that is, locally averaged velocity over a volume which is much larger than the pore but still smaller than the global size of the permeable block) in the interior of the permeable block (see figure 1), μ is the viscosity, and $\mathrm{d}p/\mathrm{d}x$ is the mean pressure gradient in the channel. Darcy's law above can be used in the absence of body forces and has been proved to be valid for a broad class of fluid flows. Beavers & Joseph suggested the following slip-boundary condition at the permeable interface to describe the interaction between the flow inside the permeable block and outer laminar channel flow (see figure 1):

$$\left.\frac{\mathrm{d}u}{\mathrm{d}y}\right|_{wall} = \frac{\alpha}{k^{1/2}}(u_{wall} - Q), \tag{9}$$

$$v_{wall} = 0, \tag{10}$$

where u and v are the velocities in the streamwise and wall-normal directions, respectively. The slip coefficient α does not depend on the viscosity of the fluid μ but depends on the structure of the permeable material at the interface between the permeable block and the flow field (Beavers, Sparrow & Masha 1974). The permeability k depends on the density of the interior region of the permeable block. Thus, the parameter $\alpha/k^{1/2}$ is not a function of the fluid property. Note that the slip-boundary condition (9) can be also interpreted as scaling of the velocity gradient at the permeable interface, based on the velocity profile within the screening depth of the permeable block (figure 1), with the characteristic length scale $k^{1/2}$ and the characteristic velocity scale $(u_{wall} - Q)$. Therefore, once the slip coefficient α is properly

chosen as a proportionality constant for such scaling, the correct slip velocity can be predicted without knowledge of the actual velocity profile and screening depth in the permeable block.

Although the slip coefficient α is difficult to measure, the slip-boundary condition (9) has been verified to properly describe the physical flow phenomena in laminar flow fields above permeable blocks by the theoretical research by Saffman (1971), numerical research by Sahraoui & Kaviany (1992), and experimental research by Gupte & Advani (1997). The importance of the slip-boundary condition (9) is that it describes a slip velocity in the main flow direction at the interface between the permeable block and the outer flow stream and is also consistent with flow phenomena.

3.2. *Boundary condition for the permeable wall in turbulent flow*

According to Beavers & Joseph (1967), there is a slip velocity u_{wall} at the interface between the main laminar flow stream and the permeable block, and this slip velocity is determined by the slip-boundary condition (9) and Darcy's law (8). For the case of turbulent flow above a permeable block, there should exist a slip-velocity condition at the permeable interface very similar to that for the case of laminar flow for the following reasons. First, in the interior of the permeable block, the characteristic length is a typical diameter of a pore, and thus the characteristic Reynolds number in the permeable block is very small. Therefore, flow in the permeable block is still expected to be laminar and to be governed by Darcy's law (8). Indeed, there may be a situation where the microscopic flow in each individual pore also becomes turbulent if the applied mean pressure gradient is very large, but we limit our interest to cases where flow in the permeable block remains laminar. Second, the slip-boundary condition at the permeable interface described in (9) is also valid for turbulent flow because the coefficients in (9), α and k, depend on the material of the permeable block, not on the flow characteristics above it. In the case of spanwise velocity (w), a similar slip-boundary condition can be defined with no mean velocity in the permeable block because there is no mean pressure gradient in the spanwise direction.

Therefore, the boundary condition at the permeable interface for turbulent flow is summarized as follows:

$$\left.\frac{\partial u}{\partial y}\right|_{wall} = \frac{\alpha}{k^{1/2}}(u_{wall} - Q), \tag{11}$$

$$\left.\frac{\partial w}{\partial y}\right|_{wall} = \frac{\alpha}{k^{1/2}} w_{wall}, \tag{12}$$

$$v_{wall} = 0, \tag{13}$$

where Q is the mean velocity in the permeable block that is given by Darcy's law (8). The boundary condition (11)–(13) together with Darcy's law (8) are non-dimensionalized with the channel half-width δ and the laminar centreline velocity u_c:

$$Q = -\frac{4Re}{\sigma^2}\frac{\mathrm{d}p}{\mathrm{d}x}, \tag{14}$$

$$\left.\frac{\partial u}{\partial y}\right|_{wall} = \frac{\alpha\sigma}{2}(u_{wall} - Q), \tag{15}$$

$$\left.\frac{\partial w}{\partial y}\right|_{wall} = \frac{\alpha\sigma}{2} w_{wall}, \tag{16}$$

$$v_{wall} = 0, \tag{17}$$

α	σ	$(k^{1/2})^+_{im}$	$(k^{1/2})^+$	$Re_{k^{1/2}}$
1	400	0.681	0.677	2.29×10^{-3}
1	200	1.363	1.328	1.76×10^{-2}
1	100	2.726	2.526	1.28×10^{-1}
1	50	5.452	4.601	8.47×10^{-1}

TABLE 1. $(k^{1/2})^+$ and $Re_{k^{1/2}}$ for various σ.

where $\sigma \equiv 2\delta/k^{1/2}$ as in Beavers & Joseph (1967). It should be mentioned here that the boundary conditions (15) and (16) should be implemented implicitly in time, e.g. $\partial w/\partial y|^{n+1}_{wall} = (\alpha\sigma/2)w^{n+1}_{wall}$ (n is the time step). An explicit treatment of the boundary condition such as $\partial w/\partial y|^{n}_{wall} = (\alpha\sigma/2)w^{n+1}_{wall}$ (that is, imposing w_{wall} at the time $t + \Delta t$ as a Dirichlet boundary condition, based on sensing $\partial w/\partial y|_{wall}$ at the time t) cannot properly reflect the flow condition at a permeable interface and completely changes the solution. For an example of the large change depending on the explicit or implicit treatment of a Neumann-type boundary condition, see the Appendix.

The boundary condition shows that the slip coefficient α and parameter σ are the primary parameters that characterize the permeable wall. According to Beavers & Joseph (1967) and Gupte & Advani (1997), changing α or σ plays the same role as changing the slip velocity at the permeable interface, as can be easily understood from (15) and (16). Within the permeable block, however, the roles of these two parameters are very different: changing the slip coefficient α may affect the screening depth of the boundary layer into the permeable block, while changing the parameter σ directly affects the velocity Q. In the present study, we are only concerned with turbulent flow above the permeable block, so we fix the slip coefficient α and change the parameter σ. This is also because α is still not completely known for a specific permeable block and a parameter setting like this is sufficient to investigate the features of turbulent channel flow above the permeable block.

The slip coefficient α is fixed to be 1 and the parameter σ varies from 400 to 50. Note that $\sigma \to \infty$ corresponds to the case of an impermeable wall. Here, special attention should be paid to the proper choice of the inverse of non-dimensionalized permeability σ. In general, pores exist on the surface as well as in the interior of a permeable block. Therefore, for the proposed boundary condition (15)–(17) to be meaningful for direct numerical simulation of turbulent flow, the typical size of a pore on the interface must be much smaller than the size of near-wall coherent structure in the wall-bounded flow. The typical diameter of a pore is often represented by the square root of the permeability, $k^{1/2}$, while the diameter of a near-wall streamwise vortex, which is known to be one of the most important near-wall structures in wall-bounded flow, is scaled in wall units. Thus, in addition to the relative length scale σ ($= 2\delta/k^{1/2}$), $(k^{1/2})^+ \equiv k^{1/2}/(\nu/u_\tau)$ should be also carefully examined. Values of $(k^{1/2})^+$ for various σ values investigated in the present study are presented in table 1, where $(k^{1/2})^+$ and $(k^{1/2})^+_{im}$ are based on the actual wall-shear velocity u_τ and the wall-shear velocity at the impermeable wall $u_{\tau_{im}}$, respectively. Since the statistical diameter d_v of near-wall streamwise vortices at low Reynolds number is $d_v^+ = 25$–30 (Kim *et al.* 1987) and thus $d_v^+ \gg (k^{1/2})^+$, the choice of the parameter σ in the present study seems to be appropriate, while the requirement is somewhat marginally satisfied in case of $\sigma = 50$. This is why our parametric study is limited to the cases with relatively large values of σ. We also performed simulations for smaller values

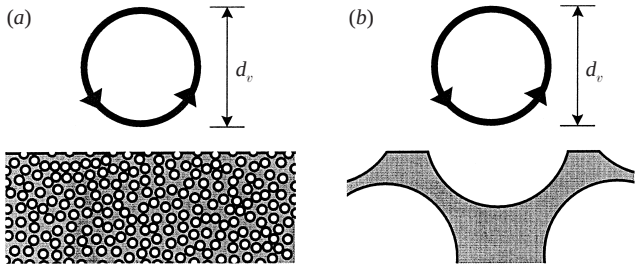

FIGURE 2. Schematic diagram of a streamwise vortex over a permeable wall: (a) $(k^{1/2})^+ \ll d_v^+$; (b) $(k^{1/2})^+ \gtrapprox d_v^+$.

of σ ($\sigma = 25$, 10 and 5) and results for those cases will be briefly mentioned in the following section, but their validity cannot be fully guaranteed. Figure 2 shows a schematic diagram of a streamwise vortex over a permeable wall in two extreme cases, $(k^{1/2})^+ \ll d_v^+$ and $(k^{1/2})^+ \gtrapprox d_v^+$. The present study considers the case of figure 2(*a*) using the direct numerical simulation technique. In case of figure 2(*b*), however, it may be possible to develop a proper boundary condition for Reynolds-averaged Navier–Stokes simulation (RANS) of turbulent flow near a permeable interface, but for direct numerical simulation coupling it with direct pore-level simulation will be a unique choice.

The pore-level Reynolds number $Re_{k^{1/2}} \equiv Qk^{1/2}/\nu$ for each σ is also presented in table 1. Note that $Re_{k^{1/2}} < 1$ in all cases. Thus, the flow inside the permeable block is thought to be laminar and Darcy's law is applicable.

4. Variations of the skin friction and mean velocity profiles

4.1. *Skin friction*

A constant mass flow rate inside the main channel (i.e. excluding the permeable-block region) is imposed for all simulations. Thus, any skin-friction change at the permeable wall would be manifested in a change in the mean pressure gradient necessary to drive the flow inside the channel with a fixed mass flow rate.

Figure 3(*a*) shows the time histories of the pressure gradient that is required to drive a fixed mass flow rate inside the channel for impermeable and permeable walls. Abrupt changes in the pressure gradient near $t = 0$ are due to the application of the slip velocity at $t = 0$. For $\sigma = 400$, the pressure gradient is nearly the same as that for impermeable walls, whereas substantial skin-friction (or, mean pressure gradient) reductions are obtained at the permeable walls for $\sigma = 200$, 100 and 50 as compared to the case of impermeable walls. With decreasing σ (i.e. increasing Q; see (14) and figure 4), the mean skin friction and skin-friction fluctuations decrease more. The amount of skin-friction reduction is listed in table 2 for each σ.

Figure 3(*b*) shows the variation of the time-averaged mean pressure gradient with respect to σ for the cases of laminar and turbulent channel flows. The solutions for laminar flow are obtained assuming that the flow is laminar at the same Reynolds number, $Re = u_c\delta/\nu = 3000$. Results for the cases of turbulent flow at $\sigma = 25, 10$ and 5 are also presented as the dashed line in figure 3. It is seen that curves for laminar and turbulent flows reach the same pressure-gradient value at $\sigma = 5$, indicating that an initial turbulent flow becomes laminar at $\sigma = 5$ (which is also evident from the parabolic mean velocity profile obtained at $\sigma = 5$), but the validity of the proposed

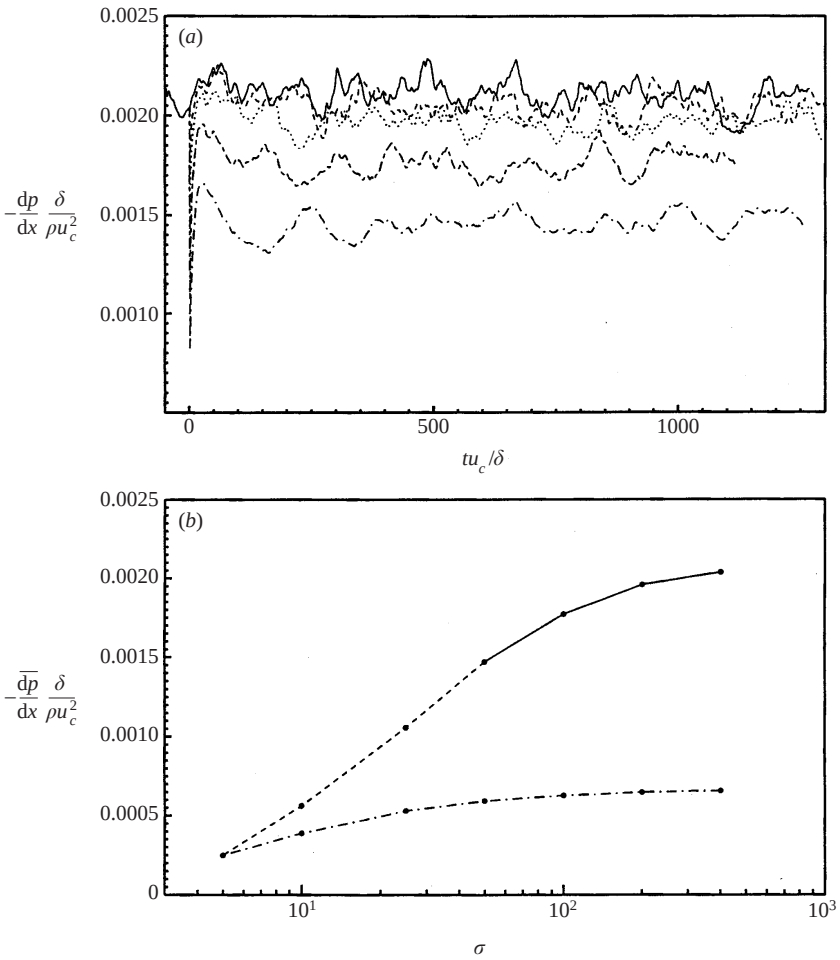

FIGURE 3. (*a*) Time history of the pressure gradient required to drive a fixed mass flow rate inside the channel: ———, impermeable wall; – – – –, $\sigma = 400$; · · · · · · ·, $\sigma = 200$; — – —, $\sigma = 100$; — · —, $\sigma = 50$; (*b*) variation of the mean pressure gradient with respect to σ: ———, turbulent flow ($\sigma \geqq 50$); – – – –, turbulent flow ($\sigma < 50$); — · —, laminar flow. ($\bar{}$) denotes the time averaging.

α	σ	$\bar{u}_{wall}/u_c$	$\bar{u}_{wall}/u_\tau$	Q/u_c	Skin-friction reduction (%)
1	400	0.031	0.681	1.53×10^{-4}	1.3
1	200	0.059	1.341	5.87×10^{-4}	5.1
1	100	0.108	2.565	2.13×10^{-3}	14.1
1	50	0.183	4.778	7.06×10^{-3}	28.8

TABLE 2. Variations of the slip velocity and skin friction with respect to σ.

boundary condition cannot be fully confirmed for such a small σ, as was already mentioned in § 3.

It might be interesting to know which of the two boundary conditions (15) and (16) plays a more important role in reducing the skin friction. Thus, we applied the

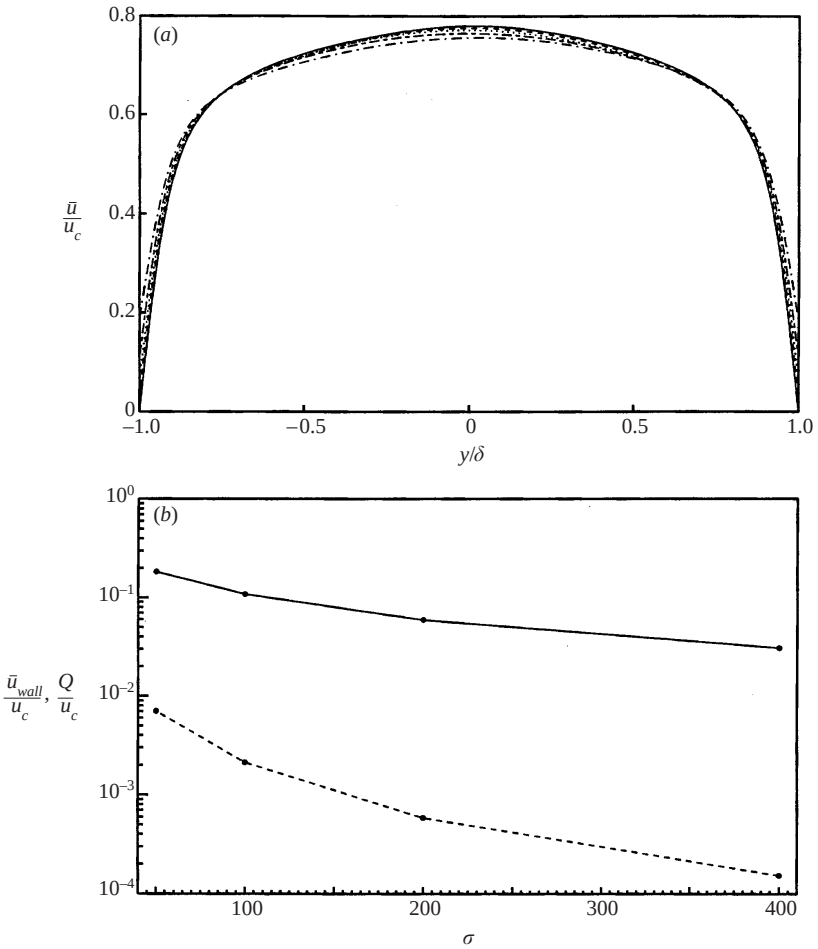

FIGURE 4. (*a*) Mean velocity profiles: ———, impermeable wall; – – – –, $\sigma = 400$; · · · · · · ·, $\sigma = 200$; — – —, $\sigma = 100$; — · —, $\sigma = 50$; (*b*) ———, mean slip velocity at the permeable wall ($\bar{u}_{wall}$); and – – – –, mean filtered velocity in the interior of the permeable block (Q).

slip-velocity boundary condition only in the spanwise direction together with $u_{wall} = 0$, resulting in 43.2% skin-friction increase for $\alpha = 1$ and $\sigma = 50$. Since application of the slip-velocity boundary condition in both the streamwise and spanwise directions provides 28.8% skin-friction decrease, we can conclude that the streamwise slip velocity plays an essential role in reducing the skin friction. Turbulence enhancement by the spanwise slip velocity seems to be significantly suppressed by the streamwise slip velocity. Without the spanwise slip velocity, the amount of skin-friction reduction became larger (39.5% reduction) than with both the streamwise and spanwise slip velocities at the same permeability, $\sigma = 50$. Therefore, the spanwise slip velocity seems to play a non-negligible role in maintaining turbulence strength even if its effect is significantly suppressed by the streamwise slip velocity.

In addition, we also examined an interesting boundary condition suggested by Perot & Moin (1995): $u_{wall} = w_{wall} = 0$ and $\partial v/\partial y|_{wall} = 0$ (see § 1). Computation issues related to this boundary condition and skin-friction variation are described in the Appendix.

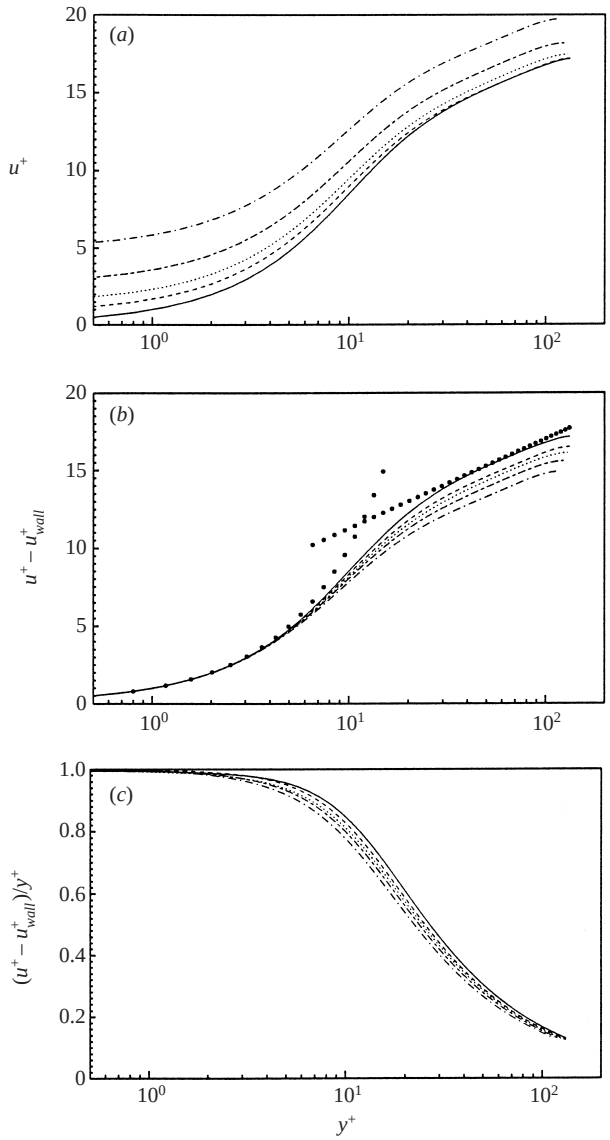

FIGURE 5. Mean velocity profiles in wall units: (*a*) u^+; (*b*) $u^+ - u^+_{wall}$; (*c*) $(u^+ - u^+_{wall})/y^+$. ———, impermeable wall; – – – –, $\sigma = 400$; · · · · · · ·, $\sigma = 200$; — – —, $\sigma = 100$; — · —, $\sigma = 50$; •, law of the wall ($u^+ = y^+$ and $u^+ = 2.5 \ln y^+ + 5.5$).

4.2. *Mean velocity profiles*

Figure 4 shows the mean velocity profiles, the mean slip velocity at the permeable wall ($\bar{u}_{wall}$) and the mean filtered velocity in the interior of the permeable block (Q). With decreasing σ, $\bar{u}_{wall}$ and Q increase (see also table 2). Also, the mean velocity gradient at the wall becomes smaller as σ decreases. Note that the mean velocity near the centreline of the channel also becomes smaller as σ decreases, to maintain the same mass flow rate as that of the initial turbulent channel flow with the impermeable wall.

The mean velocity profiles normalized by the actual wall-shear velocities are shown

σ	u_τ/u_c	$(\partial^2\bar{u}/\partial y^2\|_{wall})\delta^2/u_c$	$(\nu^2/u_\tau^3)\ \partial^2\bar{u}/\partial y^2\|_{wall}$
∞	0.0454	−8.076	−0.0096
400	0.0451	−9.109	−0.0110
200	0.0443	−10.23	−0.0131
100	0.0421	−12.03	−0.0179
50	0.0383	−12.58	−0.0248

TABLE 3. Variations of u_τ and $\partial^2\bar{u}/\partial y^2|_{wall}$ with respect to σ.

in figure 5 for both the impermeable and permeable walls, where $u^+ = \bar{u}/u_\tau$, $u^+_{wall} = \bar{u}_{wall}/u_\tau$ and $y^+ = yu_\tau/\nu$. The slopes of the log-law in the channels with the permeable walls remain about the same as in the impermeable channel, but there are upward shifts of the velocity profiles in wall units (see figure 5*a*). These upward shifts are due to the slip velocity at the permeable wall. Thus, we redraw the velocity profiles as $u^+ - u^+_{wall}$ in figure 5(*b*), which shows downward shifts in the log-law for the permeable walls. The amount of downward shift becomes larger for smaller σ. This behaviour is quite different from those observed in drag-reducing flows such as riblets (Walsh 1982; Choi, Moin & Kim 1993), active blowing/suction (Choi, Moin & Kim 1994), and polymer (Lumley 1973; Virk 1975), where upward shifts in the log-law are observed.

The downward shift in the log-law may be associated with a decrease of the viscous sublayer thickness. The Taylor series expansion yields

$$\bar{u}(y) = \bar{u}_{wall} + \left.\frac{\partial\bar{u}}{\partial y}\right|_{wall} y + \frac{1}{2}\left.\frac{\partial^2\bar{u}}{\partial y^2}\right|_{wall} y^2 + O(y^3), \tag{18}$$

which can be recast in terms of wall variables as follows:

$$u^+ = u^+_{wall} + y^+ + \frac{1}{2}\left(\frac{\nu^2}{u_\tau^3}\right)\left.\frac{\partial^2\bar{u}}{\partial y^2}\right|_{wall} y^{+2} + O(y^{+3}), \tag{19}$$

and then

$$\frac{u^+ - u^+_{wall}}{y^+} = 1 + \frac{1}{2}\left(\frac{\nu^2}{u_\tau^3}\right)\left.\frac{\partial^2\bar{u}}{\partial y^2}\right|_{wall} y^+ + O(y^{+2}). \tag{20}$$

Note that the departure from $(u^+ - u^+_{wall})/y^+ = 1$ is mainly due to the magnitudes of u_τ and $\partial^2\bar{u}/\partial y^2|_{wall}$. With decreasing σ, both u_τ and $\partial^2\bar{u}/\partial y^2|_{wall}$ monotonically decrease, resulting in a monotonic increase of $|\partial^2\bar{u}/\partial y^2|/u_\tau^3$ at the wall (see table 3). Therefore, the viscous sublayer thickness, in which $(u^+ - u^+_{wall})/y^+ \approx 1$ is satisfied, decreases more at smaller σ (see figure 5*c*). The decrease of the viscous sublayer thickness above the permeable wall is natural in the sense that the permeable wall relaxes the no-slip boundary condition at the wall which is critical in forming the viscous sublayer near the wall.

5. Turbulence statistics

In this section turbulence statistics from the calculations of turbulent channel flow with the permeable walls (σ = 200, 100 and 50) are presented and compared with those with impermeable walls.

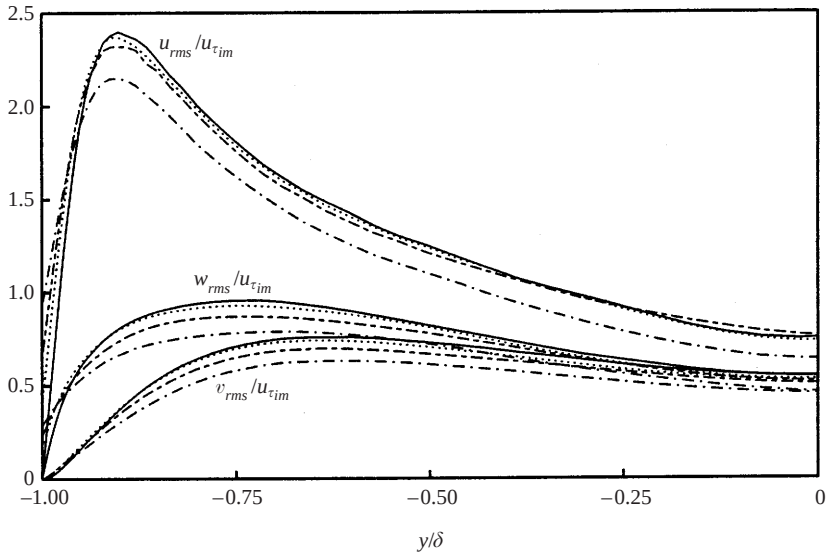

FIGURE 6. Root-mean-square velocity fluctuations normalized by the wall-shear velocity at the impermeable wall $u_{\tau_{im}}$: ———, impermeable wall; · · · · · · ·, $\sigma = 200$; — — —, $\sigma = 100$; — · —, $\sigma = 50$.

5.1. *Velocity, pressure and vorticity fluctuations*

Turbulence intensities above permeable walls normalized by the wall-shear velocity at the impermeable wall ($u_{\tau_{im}}$) are shown in figure 6, together with those above the impermeable wall. Turbulence intensities are significantly reduced by the permeable wall and they are reduced more at smaller σ. The increase of u_{rms} and w_{rms} very near the wall is due to the fluctuations of the slip velocities u_{wall} and w_{wall}. Also, from the continuity ($\partial u/\partial x|_{wall} + \partial w/\partial z|_{wall} = -\partial v/\partial y|_{wall} \neq 0$), the wall-normal velocity fluctuations above the permeable wall are slightly larger very near the wall than that above the impermeable wall.

Figure 7 shows the profile of the root-mean-square pressure fluctuations. The pressure fluctuations are substantially reduced throughout the channel due to the permeable wall. Reduction of the surface pressure fluctuations is especially notable since this implies that one can also reduce the structure-generated noise within the turbulent boundary layer. The production and dissipation of the turbulent kinetic energy also showed the same trend, indicating that the overall turbulence activity is weakened by the permeable wall.

Root-mean-square vorticity fluctuations are shown in figure 8. All three components of vorticity fluctuations are substantially reduced throughout the channel due to the permeable wall. The increase of $\omega_{y_{rms}}$ very near the wall is due to the fluctuations of the slip velocities u_{wall} and w_{wall}. It is well known that the existence of the streamwise vorticity at the impermeable wall is a kinematic result of the presence of the primary streamwise vortex above the wall and no-slip boundary condition at the wall. The y-location of the local maximum of ω_{xrms}, $y^+ \approx 20$ ($y/\delta \approx -0.85$) corresponds to the statistical location of the primary streamwise vortex above the impermeable wall. For the permeable wall, the slip-velocity condition reduces the streamwise vorticity fluctuations above the wall, and thus ω_{xrms} at the wall decreases more at smaller σ. The spanwise vorticity fluctuations at the permeable wall are also reduced due to the slip-velocity condition.

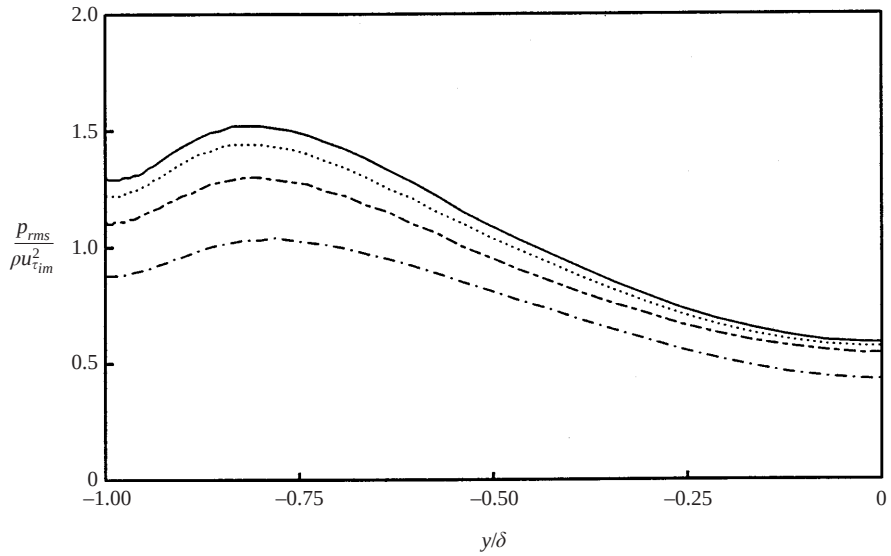

FIGURE 7. Root-mean-square pressure fluctuations normalized by the wall-shear velocity $u_{\tau_{im}}$: ———, impermeable wall; · · · · · · ·, $\sigma = 200$; — — —, $\sigma = 100$; — · —, $\sigma = 50$.

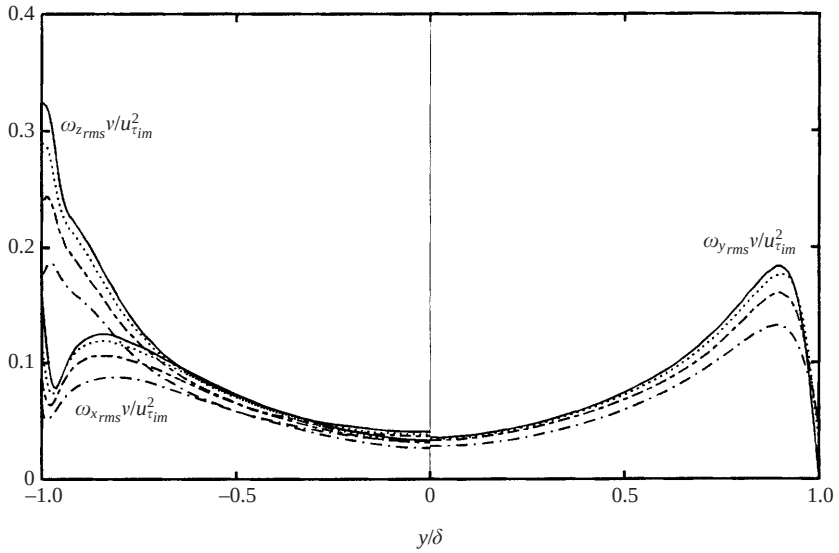

FIGURE 8. Root-mean-square vorticity fluctuations normalized by the wall-shear velocity $u_{\tau_{im}}$ and kinematic viscosity ν: ———, impermeable wall; · · · · · · ·, $\sigma = 200$; — — —, $\sigma = 100$; — · —, $\sigma = 50$.

Instantaneous streamwise and spanwise vorticities above the permeable wall ($\sigma = 50$) are shown in figure 9, together with those above the impermeable wall. It is clear that the near-wall vorticities are significantly reduced by the permeable wall. This weakened streamwise vorticity implies weakened ejection and sweep motions near the wall, which results in reduced turbulence production and Reynolds shear stress (see below). Also it is seen in figure 9(*b*) that the shear layer near the impermeable wall is significantly weakened by the slip-boundary condition of the permeable wall. The two-point correlations of the streamwise and wall-normal velocities in the span-

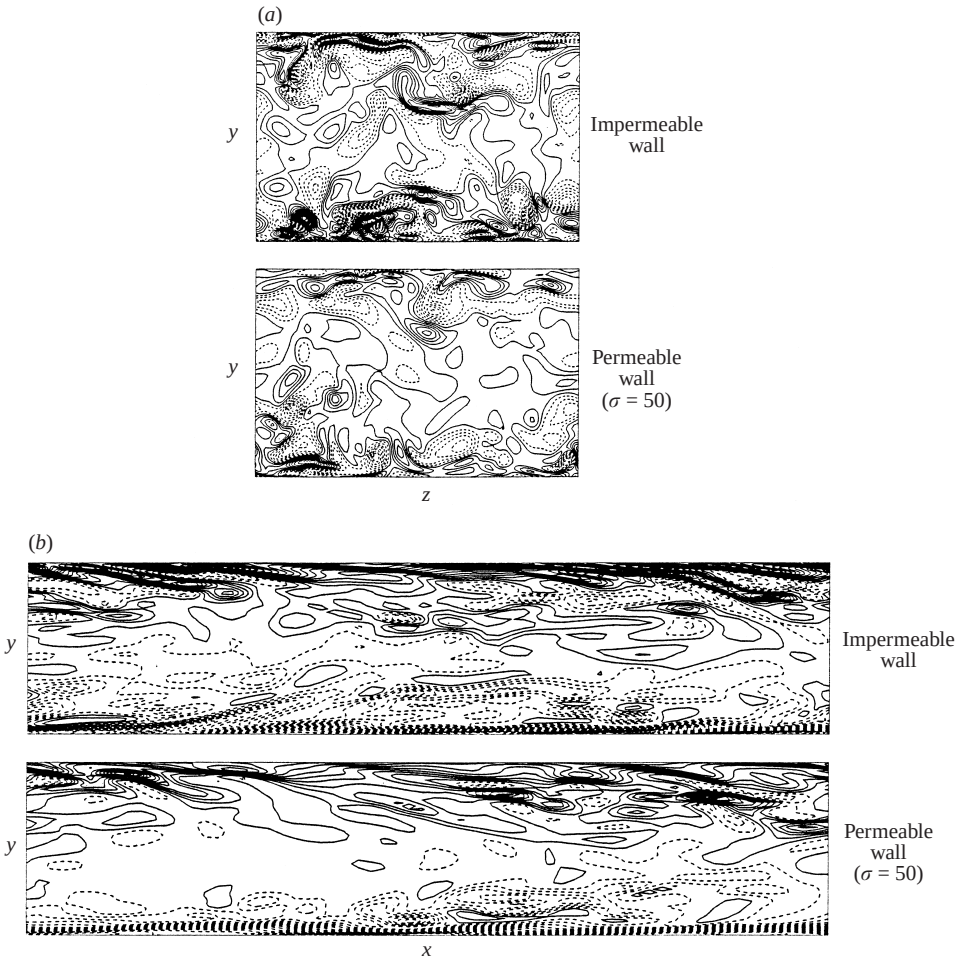

FIGURE 9. Contours of instantaneous streamwise and spanwise vorticities: (*a*) ω_x; (*b*) ω_z. The contours of $\omega_x\delta/u_{\tau_{im}}$ are from -100 to 100 in increments of 5 and those of $\omega_z\delta/u_{\tau_{im}}$ are from -300 to 300 in increments of 8.

wise direction showed that both the streak spacing and the diameter of near-wall streamwise vortices increase as σ decreases.

5.2. *Reynolds shear stress, skewness and flatness*

The Reynolds shear stress $-\overline{u'v'}$ is shown in figure 10. The total shear stress, $-\overline{u'v'} + (1/Re)\ \partial\bar{u}/\partial y$, is also shown in this figure. In the fully developed channel flow considered here, this profile should be a straight line when the flow reaches an equilibrium state. The computed results clearly indicate that this is the case. The slope of the total shear stress is reduced by the permeable wall, indicating that skin-friction reduction occurs. Also, there is a significant reduction in the Reynolds shear stress throughout the channel.

A quadrant analysis of the Reynolds shear stress (Wallace, Eckelmann & Brodkey 1972; Willmarth & Lu 1972) is performed and shown in figure 11. The second quadrant event ($u' < 0$ and $v' > 0$: ejection) and fourth quadrant event ($u' > 0$ and $v' < 0$: sweep), which contribute to the positive Reynolds shear stress, are significantly

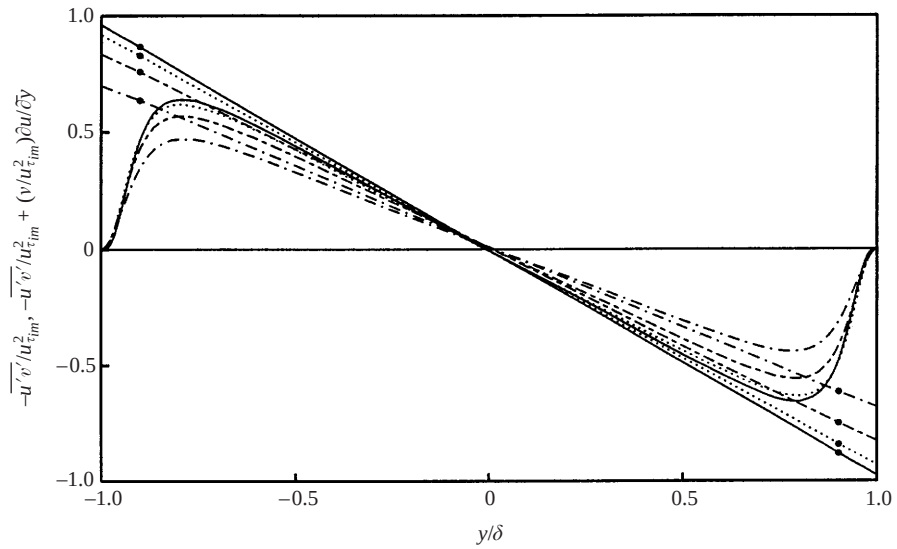

FIGURE 10. Reynolds shear stress (lines) and total shear stress (lines with •) normalized by the wall-shear velocity $u_{\tau_{im}}$: ———, impermeable wall; · · · · · · ·, $\sigma = 200$; — — —, $\sigma = 100$; — · —, $\sigma = 50$.

reduced by the permeable wall, while the changes in the first and third quadrant events are less significant.

Figure 12 shows the skewness and flatness factors of the Reynolds shear stress. For the impermeable wall, the skewness and flatness are very large near the wall and they show slight increases in magnitudes toward the centreline except near the centreline of the channel. The magnitudes of the skewness and flatness agree very well with those of Kim *et al.* (1987). For permeable walls, the skewness and flatness factors are nearly the same as those for impermeable walls except very near the wall. In the near-wall region, they are reduced more at smaller σ, meaning that the Reynolds-shear-stress-producing events near the permeable wall are less skewed and less intermittent. It is also interesting to note that the Reynolds shear stress is greatly reduced throughout the channel (figure 10), while the skewness and flatness are affected only in the near-wall region.

5.3. *Pressure–strain correlation*

Figure 13 shows diagonal elements of the pressure–strain correlation tensor

$$\phi_{ij} = \overline{p'\left(\frac{\partial u_i'}{\partial x_j} + \frac{\partial u_j'}{\partial x_i}\right)}. \tag{21}$$

These terms govern the exchange of energy among the three components of turbulent kinetic energy (Hinze 1975). The negative sign for $\phi_{\kappa\kappa}$ (no summation) indicates loss, or transfer of energy from $\overline{u_\kappa'^2}$ to other components, whereas the positive sign denotes energy gain. In the case of an impermeable wall, except in the vicinity of the wall, the streamwise velocity fluctuations transfer energy to the cross-stream velocity components. However, very near the wall, there is a large energy transfer from the wall-normal velocity component to the streamwise and spanwise velocity components. This phenomenon is referred as the splatting or impingement effect (Moin & Kim 1982).

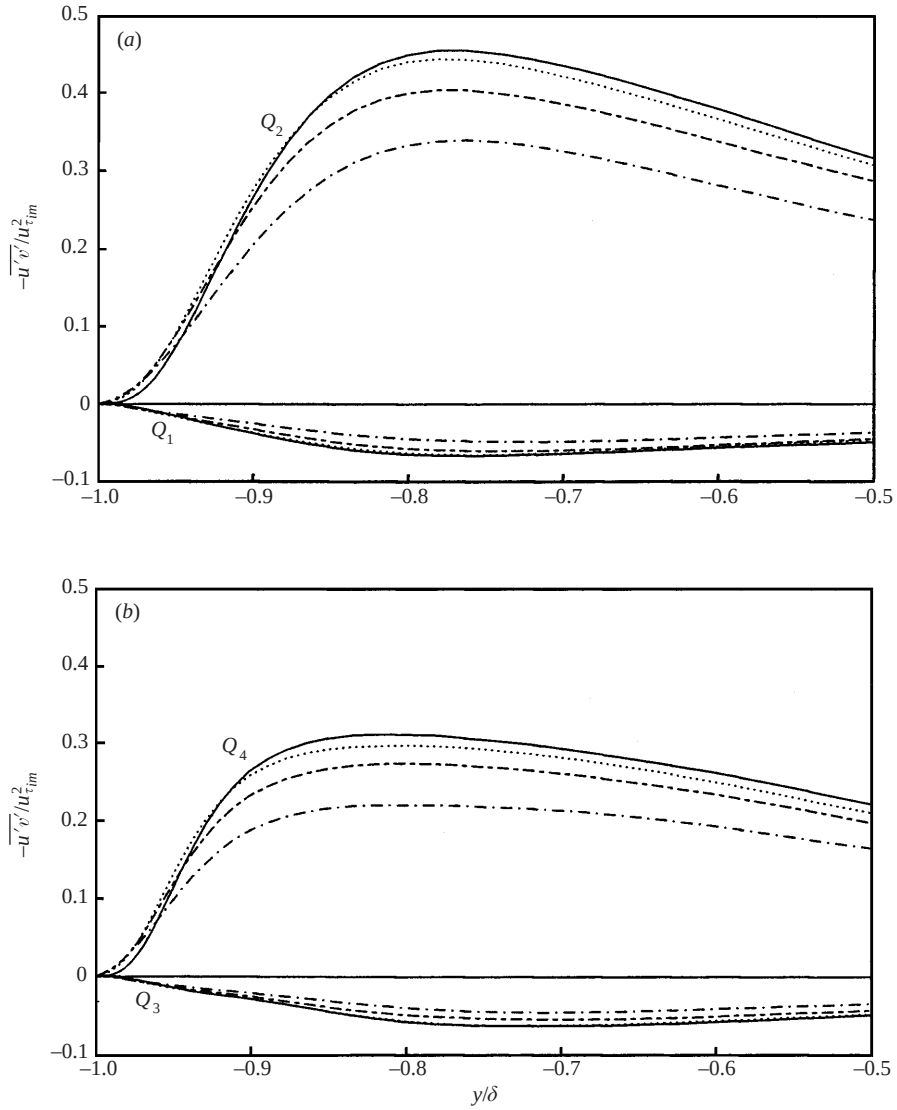

FIGURE 11. Reynolds shear stress from each quadrant normalized by the wall-shear velocity $u_{\tau_{im}}$: (*a*) first (Q_1) and second (Q_2) quadrants; (*b*) third (Q_3) and fourth (Q_4) quadrants. ———, impermeable wall; · · · · · · ·, $\sigma = 200$; — – —, $\sigma = 100$; — · —, $\sigma = 50$.

In the cases of permeable walls, the magnitudes of the pressure–strain correlations are significantly reduced throughout the channel. Interesting behaviours due to the slip-boundary condition are observed very near the wall. Due to the slip velocities, ϕ_{11}, ϕ_{22} and ϕ_{33} are not zero at the wall. Also, since the magnitude of $\partial u/\partial x|_{wall}$ is very small compared to $\partial w/\partial z|_{wall}$, $|\phi_{33}| \approx |\phi_{22}| \gg |\phi_{11}|$ at the wall. Very near the wall, energy from the wall-normal velocity component is transferred only to the spanwise velocity component, and not to the streamwise velocity component (note that $\phi_{11} < 0$ throughout the channel for permeable walls). The rate of energy transfer from the wall-normal velocity component to the spanwise component is reduced near the wall, indicating that the splatting is considerably reduced by the permeable wall.

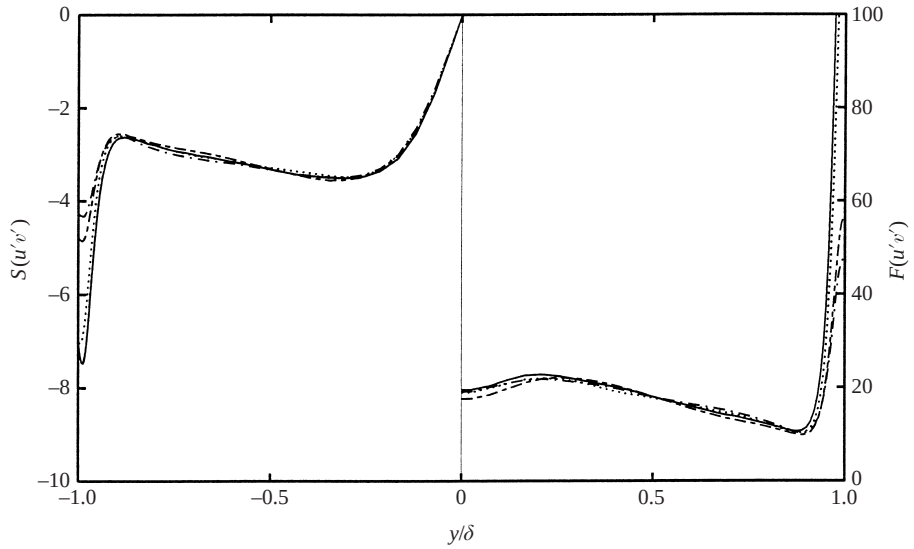

FIGURE 12. Skewness (S) and flatness (F) factors of the Reynolds shear stress: ———, impermeable wall; ·····, $\sigma = 200$; — — —, $\sigma = 100$; — · —, $\sigma = 50$.

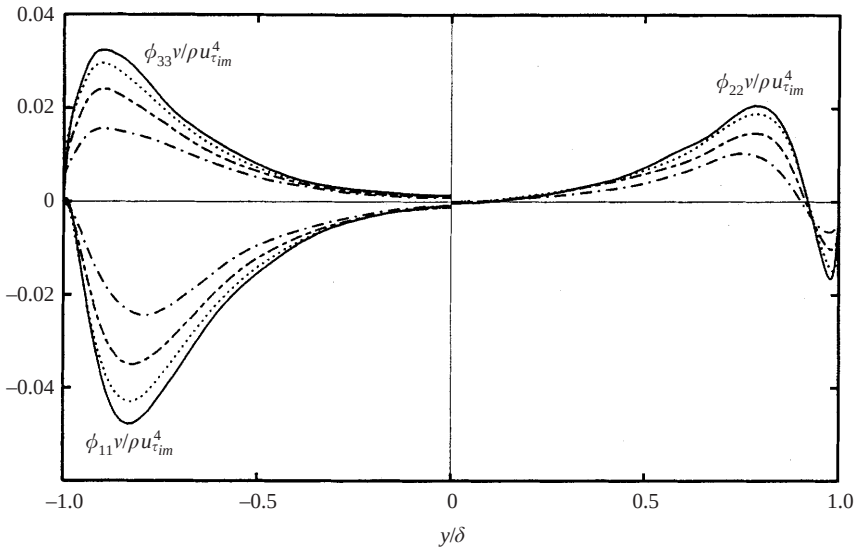

FIGURE 13. Diagonal elements of the pressure–strain correlation tensor normalized by the wall-shear velocity $u_{\tau_{im}}$: ———, impermeable wall; ·····, $\sigma = 200$; — — —, $\sigma = 100$; — · —, $\sigma = 50$.

6. Validation of the proposed boundary condition

In this section, the suitability of the boundary condition (15)–(16) proposed for the description of turbulent flow bounded by permeable walls is examined. In order to examine the validity of the proposed boundary condition, we have performed a different kind of numerical simulation, where flows inside bounding permeable blocks and turbulent channel flow between those permeable blocks are simultaneously solved (see figure 14). For brevity, hereinafter a simulation including the interior of permeable blocks as well as the main channel is denoted as CP (meaning channel and permeable

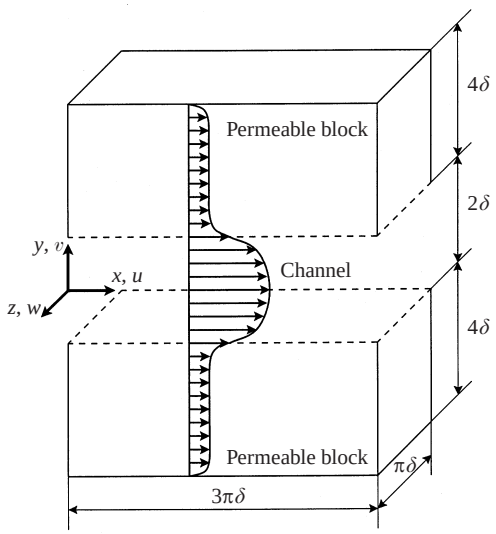

FIGURE 14. Schematic diagram of the flow geometry for simulation including permeable blocks (CP).

block), while one including only the main channel but with the proposed boundary condition (§ 3) imposed at the permeable interface is denoted as CO (meaning channel only). The proposed boundary condition (15)–(16) will be verified by comparing instantaneous velocity fields at the permeable interface obtained from CP with the proposed boundary condition. Comparison between the turbulence statistics inside the main channel obtained from CP and CO will be also shown in this section.

6.1. *Governing equation and computational detail*

For the governing equation for the flow in a permeable block, the following unsteady Brinkman's equation is chosen:

$$\rho\left(\frac{\partial u_i}{\partial t}+\frac{\partial}{\partial x_j}u_iu_j\right)=-\frac{\partial p}{\partial x_i}+\mu'\frac{\partial}{\partial x_j}\frac{\partial u_i}{\partial x_j}-\frac{\mu}{k}u_i, \tag{22}$$

$$\frac{\partial u_i}{\partial x_i}=0, \tag{23}$$

where u_i are the filtered velocity components, p is the pressure, μ is the fluid viscosity, μ' is the effective viscosity of the fluid-filled permeable medium and k is the permeability. The second term in the right-hand-side of (22) represents the flow resistance by the velocity gradient on a macroscopic scale, whereas the third term is Darcy's law that describes the average of microscopic (pore-level) flow resistance. On the other hand, inside the main channel bounded by the permeable blocks, the Navier–Stokes equations are solved and continuity of the shear stresses is assumed at the interface between the main channel and permeable block as follows (Neale & Nader 1974*a*; Kaviany 1991):

$$\mu'\left.\frac{\partial u}{\partial y}\right|_{perm}=\mu\left.\frac{\partial u}{\partial y}\right|_{chan}, \tag{24}$$

$$\mu'\left.\frac{\partial w}{\partial y}\right|_{perm}=\mu\left.\frac{\partial w}{\partial y}\right|_{chan}, \tag{25}$$

where $\partial(\cdot)/\partial y|_{perm}$ and $\partial(\cdot)/\partial y|_{chan}$ denote the gradients in the interface-normal direction at the interface, respectively evaluated within the permeable medium and the main channel. Although several ways of modelling μ' as a function of μ and/or porosity have been proposed so far, as was already mentioned in § 1, none of the models seems to provide universally satisfactory results at present. In the present study, Neale & Nader's (1974*b*) suggestion is adopted where μ' is related to the slip coefficient α of the permeable interface:

$$\mu' = \alpha^2 \mu. \tag{26}$$

Equations (22), (23) and (26) can be non-dimensionalized with the laminar centreline velocity u_c and the channel half-width δ as follows:

$$\frac{\partial u_i}{\partial t} + \frac{\partial}{\partial x_j} u_i u_j = -\frac{\partial p}{\partial x_i} + \frac{\alpha^2}{Re} \frac{\partial}{\partial x_j} \frac{\partial u_i}{\partial x_j} - \frac{\sigma^2}{4Re} u_i, \tag{27}$$

$$\frac{\partial u_i}{\partial x_i} = 0. \tag{28}$$

Note that $\alpha = 1$ in the present study and thus the effective viscosity is equal to the fluid viscosity. Therefore, the resulting governing equation will be a proper representation of the flow in a uniformly dilute porous matrix, where the property variation near the boundary is not significant. Also note that the governing equation becomes quite similar to that suggested by Vafai & Tien (1981) when the porosity is very high. They also included an empirically determined inertial term in their governing equation to handle the deviation from Darcy's law that occurs when the pore-level Reynolds number is relatively high. However, since our pore-level Reynolds number is relatively low (see table 1), we did not consider such a term in our governing equation. In the case of fully developed laminar channel flow, we confirmed that the governing equations (27) and (28) for the permeable block and the interface condition (24) for the permeable interface provide the boundary condition (15) suggested by Beavers & Joseph (1967).

The solution technique used for (27) and (28) is a semi-implicit, fractional step method and it is similar to that used for (1) and (2) (see § 2), except that the Crank–Nicolson method is used for the third term in the right-hand-side of (27). Boundary conditions and computational parameters in the streamwise and spanwise directions are identical to those in the CO case (that is, periodic boundary conditions both in the streamwise and spanwise directions and 64×96 meshes in the computational periods of $3\pi\delta \times \pi\delta$ in the streamwise and spanwise directions, respectively). The height of each permeable block is 4δ (figure 14). There are 72 non-uniform grid points in the wall-normal direction in each permeable block, while the wall-normal grid distribution inside the main channel is identical to that of simulation CO. At the permeable interface, continuity of the shear stresses, (24)–(25), and zero normal velocity, $v = 0$, are assumed, while the no-slip condition is imposed at the other boundary of each permeable block. We also applied $\mu' \, \partial v/\partial y|_{perm} = \mu \, \partial v/\partial y|_{chan}$ as an interface boundary condition for v. In this case, the simulation became unstable. The same interface condition was also applied to a laminar channel flow, providing a non-physical solution. The effect of the boundary condition for v at the permeable interface on the numerical solution has not been investigated in the literature and thus the validity of the interface boundary condition for v cannot be accurately judged from the present study. In the present study, however, we only focus on the parameter range of large σ, where $\bar{v} = 0$ and the wall-normal velocity fluctuations

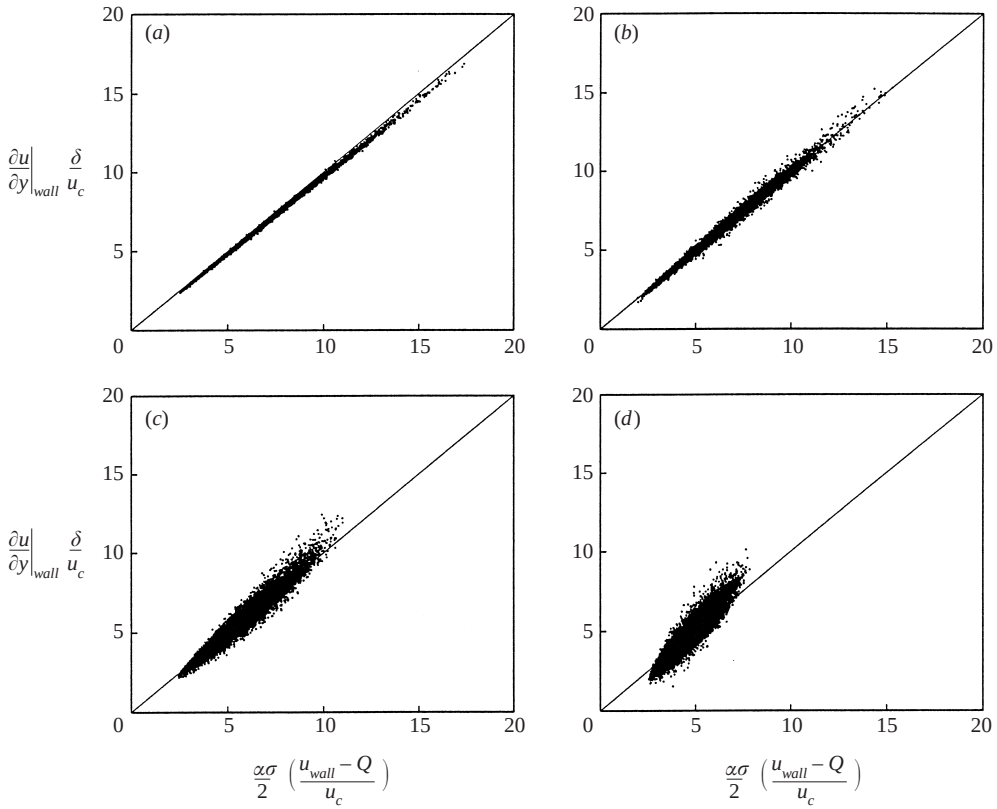

FIGURE 15. Scatter plot of $\partial u/\partial y$ versus $(\alpha\sigma/2)(u-Q)$ at the interface ($\alpha = 1$): (*a*) $\sigma = 400$; (*b*) $\sigma = 200$; (*c*) $\sigma = 100$; (*d*) $\sigma = 50$. Solid lines denote the proposed boundary condition (15).

near the permeable interface are very small. Therefore, the boundary condition used at the interface, $v = 0$, is not unreasonable.

In this section, computations are carried out with a fixed mean pressure gradient at each σ for ease of comparison between the results of CP and CO: that is, $-\mathrm{d}P/\mathrm{d}x = 2.04\times10^{-3}\rho u_c^2/\delta$, $1.96\times10^{-3}\rho u_c^2/\delta$, $1.77\times10^{-3}\rho u_c^2/\delta$ and $1.47\times10^{-3}\rho u_c^2/\delta$, respectively, for $\sigma = 400$, 200, 100 and 50. These values of $-\mathrm{d}P/\mathrm{d}x$ are obtained from figure 3(*b*). CO is performed again with the fixed mean pressure gradient for the direct comparison.

6.2. *Comparison of results*

Figures 15 and 16 are scatter plots of $\partial u/\partial y$ vs. $(\alpha\sigma/2)(u-Q)$ and $\partial w/\partial y$ vs. $(\alpha\sigma/2)w$, respectively, at the permeable interface sampled from instantaneous flow fields obtained by CP ($\alpha = 1$). The abscissae and ordinates in figures 15 and 16 correspond to the right- and left-hand sides of the proposed boundary conditions (15) and (16), respectively; (15) and (16) are also denoted by solid lines in these figures. At $\sigma = 400$ and 200, the correlations between $\partial u/\partial y|_{wall}$ and $(\alpha\sigma/2)(u_{wall}-Q)$ or $\partial w/\partial y|_{wall}$ and $(\alpha\sigma/2)w_{wall}$ are nearly perfect, and become less perfect as σ decreases but they are still high at $\sigma = 100$ and 50. These high correlations indicate that the proposed boundary conditions (15) and (16) describe the instantaneous interaction between the turbulent flow and permeable block very well and thus they are suitable for direct numerical simulation of turbulent flow over a permeable wall.

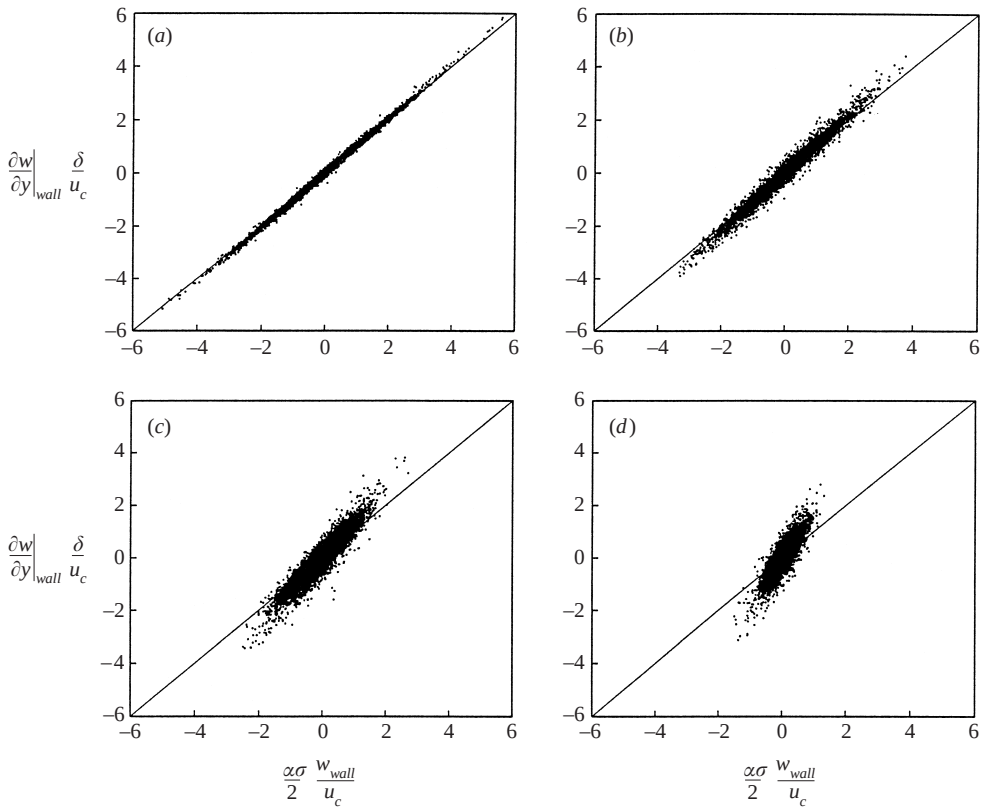

FIGURE 16. Scatter plot of $\partial w/\partial y$ versus $(\alpha\sigma/2)w$ at the interface ($\alpha = 1$): (*a*) $\sigma = 400$; (*b*) $\sigma = 200$; (*c*) $\sigma = 100$; (*d*) $\sigma = 50$. Solid lines denote the proposed boundary condition (16).

Figure 17 shows the root-mean-square velocity and vorticity fluctuations above the permeable interface obtained by CP and CO. Results obtained from two different simulations showed excellent agreement with each other for $\sigma = 400$, 200 and 100 (see, for example, figure 17*a*), which is natural considering the strong correlations shown in figures 15 and 16. It is interesting that results at $\sigma = 50$ agree fairly well with each other although the correlation at $\sigma = 50$ is not as strong as for $\sigma \geqq 100$. For $\sigma < 50$, the agreement between the results from two different simulations (CP and CO) became worse, which may be due to $(k^{1/2})^+ \gtrapprox d_v^+$ in these cases as described in § 3.2.

7. Summary

The objectives of the present study were to suggest a proper boundary condition at the interface between turbulent channel flow and a permeable block, and to investigate the turbulence characteristics above the permeable wall. The boundary condition suggested was an extended version of Beavers & Joseph's (1967), who suggested a slip velocity in the streamwise direction in laminar channel flow with permeable walls.

In the suggested slip-boundary condition (14)–(17), there are two parameters α and σ. The parameter α may be associated with the screening depth of the boundary layer into the permeable block, while σ is directly related to the mean filtered velocity in

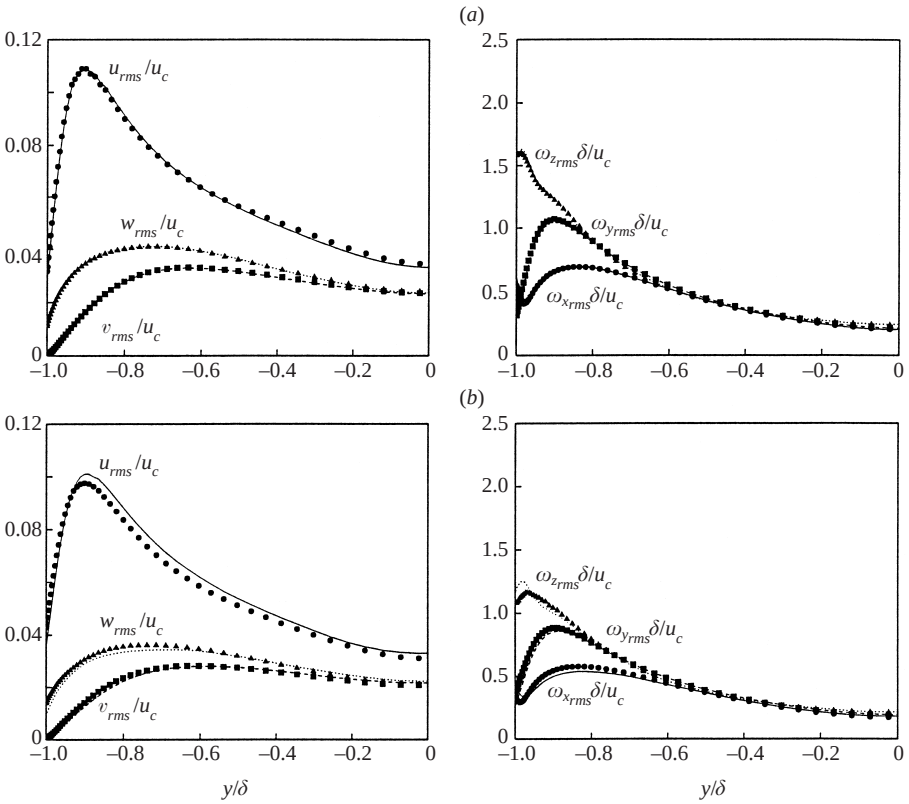

FIGURE 17. Root-mean-square velocity and vorticity fluctuations: (*a*) $\sigma = 100$; (*b*) $\sigma = 50$. Lines are from the simulation including permeable blocks (CP) and symbols are from the simulation with the proposed boundary conditions (15) and (16) (CO).

the permeable block (Beavers & Joseph 1967). Since we were mainly concerned with the flow above the permeable block, we fixed α to be 1 and varied σ ($\sigma = 400$, 200, 100 and 50) in the present study. Here, $\sigma \to \infty$ corresponds to an impermeable wall. With the slip-boundary condition suggested at the permeable wall, direct numerical simulations of turbulent channel flow bounded by the permeable wall were performed.

Significant skin-friction reductions at the interface were observed in the presence of permeable walls. The amount of skin-friction reduction became larger at smaller σ (larger mean filtered velocity in the permeable block). The same trend was also observed in laminar channel flow (Beavers & Joseph 1967) and this is consistent with many other experiments on laminar flow over permeable walls. The mean velocity profiles normalized by the actual wall-shear velocities showed that the slopes of the log-law remained about the same as in the impermeable channel, but there was downward shift in $u^+ - u^+_{wall}$ vs. y^+. These downward shifts were associated with the reduced viscous sublayer thickness in the presence of permeable walls. A decrease of the viscous sublayer thickness above the permeable wall is natural because the permeable wall relaxes the no-slip boundary condition at the wall which is critical in forming the viscous sublayer near the wall.

Turbulence intensities and pressure fluctuations above the permeable wall decreased further at smaller σ except very near the wall. The increase of some turbulence quantities there was due to the slip-velocity fluctuations at the permeable wall.

The decrease of the wall pressure fluctuations is notable since the permeable wall may be used to reduce the flow-induced noise in turbulent boundary layer. The Reynolds shear stress and vorticity fluctuations above the permeable wall were also significantly reduced. The weakened streamwise vorticity fluctuations imply weakened ejection and sweep motions near the wall, which is also associated with reduced turbulence production and Reynolds shear stress. The pressure–strain correlations showed that the energy transfer among the three velocity components was suppressed by the permeable wall. Also, the splatting near the wall was significantly attenuated in the presence of the permeable wall.

For the validation of the proposed boundary condition, simulations using both the Brinkman equation for the interior of the permeable block and the Navier–Stokes equation for the main channel were performed and the results were compared with those of simulations using the Navier–Stokes equation for the main channel together with the proposed boundary condition at the permeable wall. Results (turbulence statistics inside the main channel as well as instantaneous velocities at the permeable interface) from the two different simulations agreed very well with each other for the range of σ investigated in this study ($\sigma \geqq 50$) and thus the proposed boundary condition is thought to be suitable for direct numerical simulation of turbulent flow over a permeable wall.

This work is sponsored by the Creative Research Initiatives through the Korean Ministry of Science and Technology.

Appendix. Boundary condition suggested by Perot & Moin (1995) for a 'perfectly' permeable wall

Recently, Perot & Moin (1995) investigated turbulent flow over a 'perfectly' permeable wall to study the blocking effect of a no-slip wall. They allowed the fluid to freely permeate through the surface, i.e. $\partial v/\partial y = 0$ rather than $v = 0$ on the wall. Thus the complete boundary condition at the wall is

$$u_{wall} = w_{wall} = 0, \qquad \left.\frac{\partial v}{\partial y}\right|_{wall} = 0. \tag{A 1}$$

In the present study, the boundary condition (A 1) is applied to turbulent channel flow. The main difficulty of applying (A 1) to channel flow is how to computationally implement $\partial v/\partial y|_{wall} = 0$. We apply three different methods as follows:

$$v_{wall}^{n+1} = v_1^n, \tag{A 2}$$

$$v_{wall}^{n+1} = v_1^{n+1}, \tag{A 3}$$

$$v_{wall}^{n+1} = C_1 v_1^{n+1} + C_2 v_2^{n+1}, \tag{A 4}$$

where n is the time step, and v_1 and v_2 are the wall-normal velocities nearest to the wall (see figure 18). The boundary condition (A 2) is an explicit treatment of $\partial v/\partial y|_{wall} = 0$. Thus, $\partial v/\partial y|_{wall}^{n+1} = 0$ is not completely satisfied. The boundary condition (A 3) is an implicit treatment of $\partial v/\partial y|_{wall} = 0$. Thus $\partial v/\partial y|_{wall}^{n+1} = 0$. However, in a staggered mesh system, this boundary condition produces a non-negligible numerical error because it implies $\partial u/\partial x + \partial w/\partial z = 0$ in the first numerical cell from continuity, which is not physically correct. Thus, we use a three-point extrapolation scheme of second-order

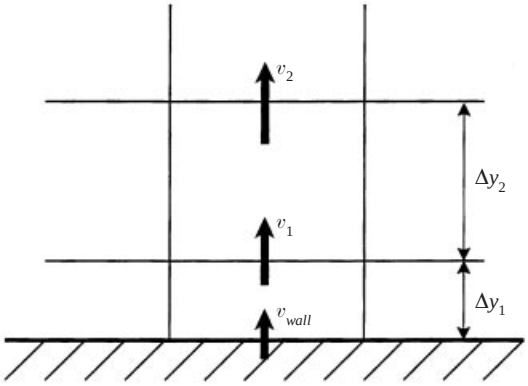

FIGURE 18. Schematic diagram of the staggered mesh system near the wall.

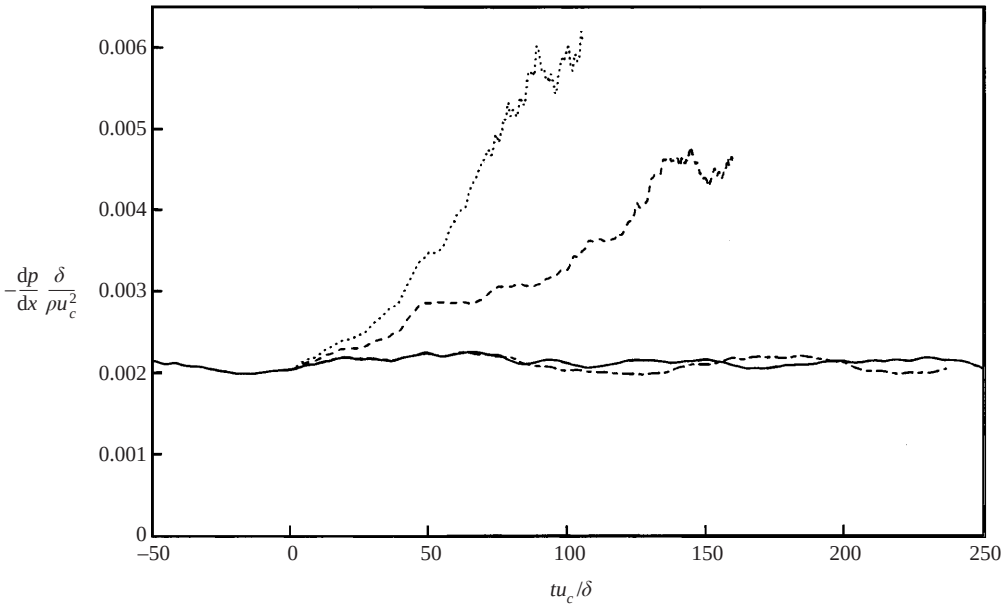

FIGURE 19. Time history of the pressure gradient required to drive a fixed mass flow rate: ———, impermeable wall; – – – –, (A 2); · · · · · · ·, (A 3); — — —, (A 4).

accuracy for $\partial v/\partial y|_{wall}^{n+1} = 0$, which is (A 4). Here, $C_1 = (\Delta y_1 + \Delta y_2)^2/(2\Delta y_1 \Delta y_2 + \Delta y_2^2)$ and $C_2 = -\Delta y_1^2/(2\Delta y_1 \Delta y_2 + \Delta y_2^2)$ (see figure 18).

Each of three different methods (A 2)–(A 4) is applied to turbulent channel flow and its skin-friction variation is shown in figure 19. Surprisingly, the results are completely different. The skin frictions due to (A 2) and (A 3) significantly increase compared to the no-slip wall, while in the case of (A 4) it is nearly the same as that of the no-slip wall. The root-mean-square wall-normal velocity fluctuations at the wall are shown in figure 20. The velocity fluctuations at the wall significantly increase when (A 2) and (A 3) are applied, but are very small in the case of (A 4). The skin-friction increase by applying (A 1) to turbulent pipe flow was reported in Wagner & Friedrich (1997), but their numerical scheme for (A 1) was not explicitly specified in the paper.

As was shown by Beavers & Joseph (1967) and also by the present study, the skin friction is significantly decreased by the slip-boundary condition (14)–(17) at the

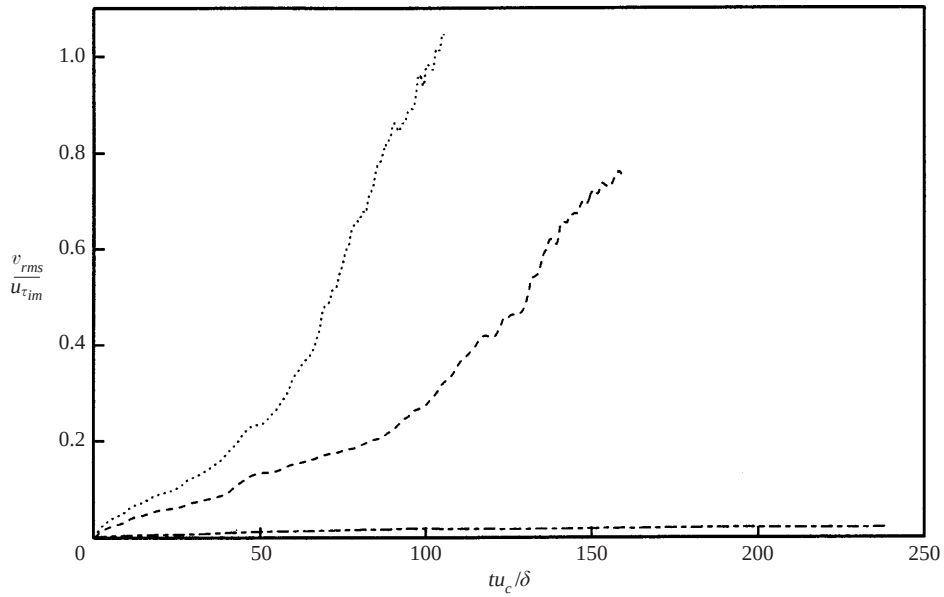

FIGURE 20. Root-mean-square wall-normal velocity fluctuations at the wall normalized by the wall-shear velocity $u_{\tau_{im}}$: – – – –, (A 2); · · · · · · ·, (A 3); — – —, (A 4).

permeable wall. Thus, the boundary condition used by Perot & Moin (1995) describes a completely different turbulent flow field from ours, although both studies use the same terminology for 'permeable wall'.

REFERENCES

ANTOHE, B. V. & LAGE, J. L. 1997 A general two-equation macroscopic turbulence model for incompressible flow in porous media. *Intl J. Heat Mass Transfer* **40**, 3013.

BEAVERS, G. S. & JOSEPH, D. D. 1967 Boundary conditions at a naturally permeable wall. *J. Fluid Mech.* **30**, 197.

BEAVERS, G. S., SPARROW, E. M. & MASHA, B. A. 1974 Boundary condition at a porous surface which bounds a fluid flow. *AIChE J.* **20**, 596.

BRINKMAN, H. C. 1947 A calculation of the viscous force exerted by a flowing fluid on a dense swarm of particles. *Appl. Sci. Res.* **1**, 27.

CHOI, H. & MOIN, P. 1994 Effects of the computational time step on numerical solutions of turbulent flow. *J. Comput. Phys.* **113**, 1.

CHOI, H., MOIN, P. & KIM, J. 1992 Turbulent drag reduction: studies of feedback control and flow over riblets. *Rep.* TF-55. Department of Mechanical Engineering, Stanford University.

CHOI, H., MOIN, P. & KIM, J. 1993 Direct numerical simulation of turbulent flow over riblets. *J. Fluid Mech.* **255**, 503.

CHOI, H., MOIN, P. & KIM, J. 1994 Active turbulence control for drag reduction in wall-bounded flows. *J. Fluid Mech.* **262**, 75.

GUPTE, S. K. & ADVANI, S. G. 1997 Flow near the permeable boundary of a porous medium: An experimental investigation using LDA. *Exps. Fluids* **22**, 408.

HINZE, J. O. 1975 *Turbulence*, 2nd Edn. McGraw-Hill.

KAVIANY, M. 1987 Boundary-layer treatment of forced convection heat transfer from a semi-infinite flat plate embedded in porous media. *ASME: Trans. J. Heat Transfer* **109**, 345.

KAVIANY, M. 1991 *Principles of Heat Transfer in Porous Media.* Springer.

KIM, J. & MOIN, P. 1985 Application of a fractional-step method to incompressible Navier–Stokes equations. *J. Comput. Phys.* **59**, 308.

KIM, J., MOIN, P. & MOSER, R. 1987 Turbulence statistics in fully developed channel flow at low Reynolds number. *J. Fluid Mech.* **177**, 133.

KOPLIK, J., LEVINE, H. & ZEE, A. 1983 Viscosity renormalization in the Brinkman equation. *Phys. Fluids* **26**, 2864.

LE, H. & MOIN, P. 1991 An improvement of fractional step methods for the incompressible Navier–Stokes equations. *J. Comput. Phys.* **92**, 369.

LUMLEY, J. L. 1973 Drag reduction in turbulent flow by polymer additives. *J. Polymer Sci.* D: *Macromol. Rev.* **7**, 263.

LUNDGREN, T. S. 1972 Slow flow through stationary random beds and suspensions of spheres. *J. Fluid Mech.* **51**, 273.

MOIN, P. & KIM, J. 1982 Numerical investigation of turbulent channel flow. *J. Fluid Mech.* **118**, 341.

NEALE, G. H. & NADER, W. K. 1974*a* Prediction of transport process within porous media: creeping flow relative to a fixed swarm of spherical particles. *AIChE J.* **20**, 530.

NEALE, G. H. & NADER, W. K. 1974*b* Practical significance of Brinkman extension of Darcy's law: coupled parallel flows within a channel and a bounding porous medium. *Can. J. Chem. Engng* **52**, 475.

PEROT, B. & MOIN, P. 1995 Shear-free turbulent boundary layers. Part 1. Physical insights into near-wall turbulence. *J. Fluid Mech.* **295**, 199.

SAFFMAN, P. G. 1971 On the boundary condition at the surface of a porous medium. *Stud. Appl. Maths* **50**, 93.

SAHRAOUI, M. & KAVIANY, M. 1992 Slip and no-slip velocity boundary conditions at interface of porous, plain media. *Intl J. Heat Mass Transfer* **35**, 927.

SLATTERY, J. C. 1969 Single-phase flow through porous media. *AIChE J.* **15**, 866.

VAFAI, K. & TIEN, C. L. 1981 Boundary and inertia effects on flow and heat transfer in porous media. *Intl J. Heat Mass Transfer* **24**, 195.

VIRK, P. S. 1975 Drag reduction fundamentals. *AIChE J.* **21**, 625.

WAGNER, C. & FRIEDRICH, R. 1997 On the turbulence structure in solid and permeable pipes. In *Proc. Eleventh Symp. on Turbulent Shear Flows*, vol. 3, pp. 33-19–33-24.

WALLACE, J. M., ECKELMANN, H. & BRODKEY, R. S. 1972 The wall region in turbulent shear flow. *J. Fluid Mech.* **54**, 39.

WALSH, M. J. 1982 Turbulent boundary layer drag reduction using riblets. *AIAA Paper* 82-0169.

WHITAKER, S. 1986 Flow in porous media I: a theoretical derivation of Darcy's law. *Transp. Porous Media* **1**, 3.

WILLMARTH, W. W. & LU, S. S. 1972 Structure of the Reynolds stress near the wall. *J. Fluid Mech.* **55**, 65.